Materials Today 96 (2026) 103329

Contents lists available at ScienceDirect

Materials Today

journal homepage: www.elsevier.com/locate/mattod

Ultra-strong and ductile low-alloy titanium by additive manufacturing

Chuanxi Ren [a,b,1], Hao Wang [c,d,1], Xiangyuan Cui [c,d], Jinjin Guo [e], Hansheng Chen [c,d], Zizheng Song [a,b], Hengchao Shi [a,b], Yating Ran [a,b], Chunjin Wang [a], Chi Fai Cheung [a], Hongwei Liu [d], Kang Cheung Chan [a,b], Xiaozhou Liao [c,d], Ting Zhu [f,*], Dengke Chen [e,*], Simon P. Ringer [c,d,*], Zibin Chen [a,b,*]

[a] State Key Laboratory of Ultra-precision Machining Technology, Department of Industrial and Systems Engineering, The Hong Kong Polytechnic University, Hong Kong 999077, China
[b] Research Institute for Advanced Manufacturing, Department of Industrial and Systems Engineering, The Hong Kong Polytechnic University, Hong Kong 999077, China
[c] School of Aerospace, Mechanical and Mechatronic Engineering, The University of Sydney, New South Wales 2006, Australia
[d] Australian Centre for Microscopy & Microanalysis, The University of Sydney, New South Wales 2006, Australia
[e] Department of Engineering Mechanics, School of Ocean and Civil Engineering, Shanghai Jiao Tong University, Shanghai 200240, China
[f] Woodruff School of Mechanical Engineering, Georgia Institute of Technology, Atlanta, GA 30332, USA

ARTICLE INFO

Keywords:
Additive manufacturing
High-strength low-alloy Ti
Hierarchical microstructure
Shearable coherent nanoprecipitate
Superior strength–ductility synergy

ABSTRACT

Strong yet ductile Ti alloys are crucial for aerospace and biomedical applications. While low-alloy Ti systems reduce dependence on expensive alloying elements, they often suffer from poor mechanical performance. We demonstrate the development of high-strength low-alloy (HSLA) Ti by leveraging the highly non-equilibrium processing conditions of additive manufacturing to control diffusive phase transformations. This approach enables the formation of hierarchical microstructures in Ti-Cu alloys, featuring micron-sized grains with refined laths and finely dispersed nanoprecipitates. The resulting structural hierarchy effectively impedes dislocation glide and promotes multislips, delivering ultra-high strength without compromising ductility. A Ti-5Cu alloy with dual nanoprecipitation achieves an exceptional ultimate tensile strength of 1,340 MPa and 12% elongation to failure, outperforming most commercial Ti alloys. These results highlight the transformative potential of additive manufacturing to develop more sustainable Ti systems that are strong, ductile, low-alloyed, and cost-effective.

Introduction

Titanium (Ti) alloys are widely used in aerospace and biomedical fields due to their excellent specific strength, fatigue life, corrosion resistance, and biocompatibility [1]. Inspired by the success of high-strength low-alloy (HSLA) steels, which to achieve a balance of high strength and ductility through thermomechanical processing [2]. The concept of high-strength low-alloy (HSLA) materials was originally developed for steels and has been widely used for decades. In steels, HSLA grades typically contain relatively small amounts of alloying elements, generally around or below 5 wt%. For example, the total alloying contents in typical HSLA steels such as AISI 4340, 30CrNiMo8, and AISI 4330V are approximately 5 wt%, 5.5 wt%, and 5 wt% (Tables S1-S3), respectively [3–5]. In contrast, the mechanical properties of Ti alloys, particularly yield strength (YS), ultimate tensile strength (UTS), and total elongation (TE), are highly sensitive to both the type and concentration of alloying elements, with alloy content playing a dominant role. As summarized in Table S4, α-Ti alloys typically contain less than 10 wt% alloying elements but generally exhibit relatively low strength [6]. Achieving higher strength in Ti alloys usually requires significantly greater alloy additions. Near-α, α + β, and β-Ti alloys commonly contain more than 10 wt% alloying elements, which contribute to their enhanced YS and UTS. In practice, attaining a UTS of ~800 MPa or higher in conventional Ti alloys almost always relies on relatively high alloying content.

Extending the concept to HSLA to Ti offers a promising pathway for

* Corresponding authors.
E-mail addresses: ting.zhu@me.gatech.edu (T. Zhu), dengke.chen@sjtu.edu.cn (D. Chen), simon.ringer@sydney.edu.au (S.P. Ringer), zi-bin.chen@polyu.edu.hk (Z. Chen).
[1] These authors contributed equally to this work.

https://doi.org/10.1016/j.mattod.2026.103329
Received 10 September 2025; Received in revised form 1 April 2026; Accepted 2 April 2026
Available online 7 April 2026

developing strong, ductile, and cost-effective Ti alloys. Motivated by this contrast with steels, we introduce the concept of HSLA-Ti, defined as titanium alloys with total alloying additions around or below 5 wt%, while still delivering high performance. Specifically, we propose that HSLA-Ti alloys should meet the criteria of UTS > 800 MPa and total elongation (TE) > 10% [7,8]. This definition parallels the design principles of HSLA steels and highlights a pathway toward titanium alloys that are simultaneously strong, ductile, and cost-effective, enabling widespread structural applications [9,10]. Finally, we note that the notion of a 'low alloy' regime of ≤ 5 wt% might seem rather wider than the low alloy regime in steels. Nevertheless, we consider this concept to be valuable because so much attention is focused on compositionally complex alloys (otherwise known as high entropy alloys) where there are either equiatomic amounts of alloying elements or large additions ≥ 10 at.% involved. This brings extra context for our preference around the notion of HSLA Ti alloys. Current commercial Ti alloys, such as Ti-6Al-4V (Ti-6-4), Ti-6Al-6V-2Sn (Ti-6-6-2), Ti-6Al-2Sn-4Zr-6Mo (Ti-6-2-4-6), Ti-6Al-2Sn-2Zr-2Mo-2Cr-0.15Si (Ti-6-2-2-2-2), combine attractive strength and ductility but are expensive and challenging to produce [11]. In contrast, low-alloy Ti variants, such as commercially pure (CP)-Ti, Ti-Al, Ti-Cu, Ti-Cr, Ti-Fe, and Ti-Mo, are cheaper and easier to process, but they often have inferior mechanical properties [12]. For instance, Ti-3Fe and Ti-5Cr improve UTS (~670 MPa and 750 MPa, respectively) but reduce elongation to failure (15% and 10%, respectively) [13,14], compared to CP-Ti (UTS ~340 MPa and elongation 34%) [15]. Although cast Ti-Cu alloys offer high strength (~890 MPa), their low ductility (~1%) [16] limits industrial applications.

The poor tensile properties in low-alloy Ti stem largely from the presence of large, high-density incoherent secondary phases. For instance, Ti_3Al precipitates form in Ti-Al alloys, Ti_2Cu in Ti-Cu alloys, brittle β flakes in Ti-Fe alloys, and the brittle ω phase in Ti-Cr alloys [7,17–19]. These precipitates and secondary phases act as stress concentrators, significantly reducing tensile ductility. To improve the mechanical properties of Ti alloys, finely dispersed coherent precipitates are preferred. Achieving this usually involves non-equilibrium shearable phases, which enhance strength and maintain ductility by promoting dislocation blocking and multiplication during plastic deformation [20]. However, generating microstructures with finely dispersed metastable shearable phases is challenging, as alloying elements in Ti tend to form large, stable equilibrium phases due to their high diffusion rates.

Additive manufacturing (AM), such as laser-powder bed fusion (L-PBF), involves highly localized melting, rapid cooling and reheating, producing significant thermal gradients compared to traditional manufacturing. AM has emerged as an effective method for introducing non-equilibrium phases and structures into metallic materials [21]. Its local, rapid cooling limits solute diffusion, promoting non-equilibrium phases over those in equilibrium phase diagrams [22]. This study focuses on binary Ti-Cu alloys, exploiting the high diffusion rate and low solubility of Cu in Ti at room temperature. We leverage AM to create hierarchical microstructures in Ti-Cu alloys, simultaneously achieving refined α′ (or α) laths, high-density non-equilibrium (η′) and equilibrium (η Ti_2Cu) nanoprecipitates—termed dual nanoprecipitation—in a low-alloy Ti system. The η′ phase, rarely formed in this system, enables simultaneous strengthening without loss of ductility. By introducing the HSLA concept to Ti, this study establishes a cost-effective microstructural design strategy that achieves mechanical performance comparable to or exceeding that of conventional high-alloy α-type Ti.

Results

Exceptional mechanical properties

Bulk Ti-Cu alloy specimens (Ti-1.5Cu, Ti-3Cu, Ti-5Cu, and Ti-7Cu by weight percentage) were fabricated using L-PBF with mechanically

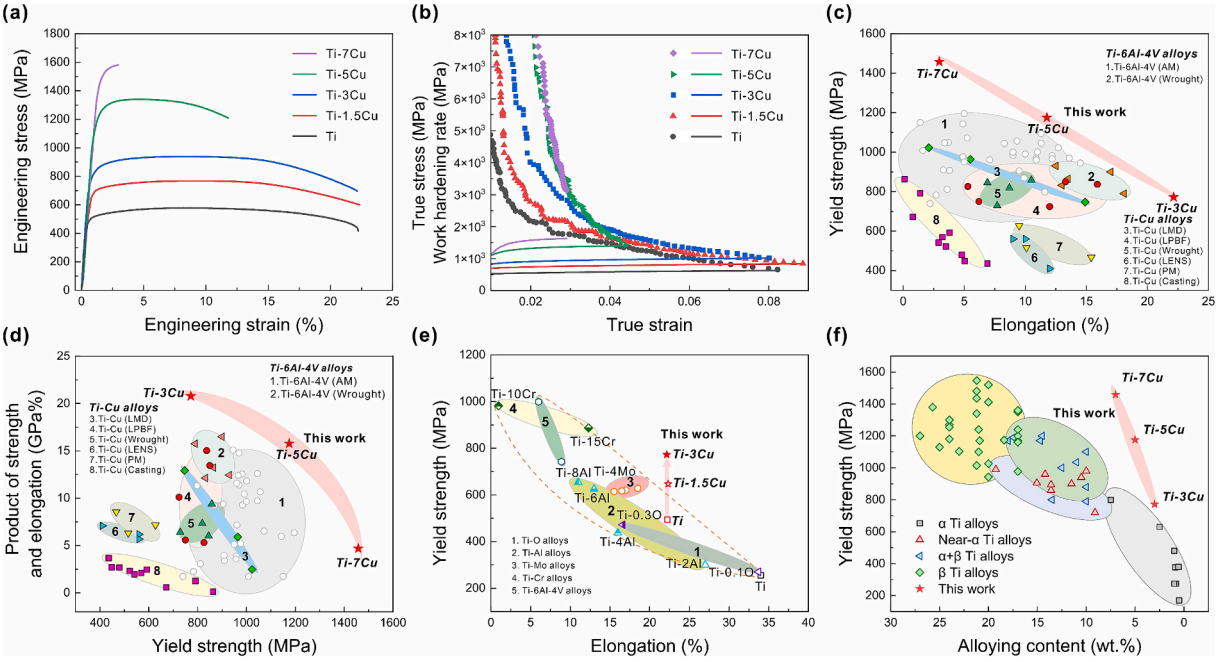

Fig. 1. Mechanical properties of HSLA Ti fabricated by additive manufacturing. (a) Engineering stress–strain curves of Ti, Ti-1.5Cu, Ti-3Cu, Ti-5Cu, and Ti-7Cu alloys. (b) True stress vs. true strain curves and corresponding work hardening rate as a function of true strain for Ti, Ti-1.5Cu, Ti-3Cu, Ti-5Cu, and Ti-7Cu alloys. (c) Comparison of the yield strength vs. total elongation of Ti-3Cu, Ti-5Cu, and Ti-7Cu alloys in this work with other Ti-Cu alloys fabricated by multiple technologies [16,26–33], and Ti-6Al-4V alloys fabricated by multiple AM and wrought technologies [34–38]. LMD, LENS, and PM denote laser metal deposition, laser engineered net shaping, and powder metallurgy, respectively. (d) Comparison of the strength-ductility product vs. yield strength for as-printed Ti-Cu alloys in this work and Ti-6Al-4V alloy and Ti-Cu alloys fabricated by multiple technologies [16,26–38]. (e) Comparison of the yield strength vs. total elongation of Ti, Ti-1.5Cu, and Ti-3Cu in this work with typical binary Ti alloys (Ti-O, Ti-Al, Ti-Mo, and Ti-Cr) and ternary alloy (Ti-6Al-4V) fabricated by traditional casting and wrought techniques [14,39–43]. (f) Comparison of the yield strength vs. alloy content of Ti-3Cu, Ti-5Cu, and Ti-7Cu alloys in this work with common α, near-α, α + β, and β Ti alloys [12,44–48].

mixed powders of CP-Ti and Cu. Fig. 1 a and Fig. S6, along with Table S5, present the tensile properties of L-PBF Ti and Ti-Cu alloys. CP-Ti exhibited a UTS of ~580 MPa and tensile ductility of ~22% elongation to failure. In contrast, Ti-Cu alloys demonstrated significant UTS improvements: Ti-1.5Cu and Ti-3Cu reached ~770 MPa and ~940 MPa, respectively, without sacrificing tensile ductility. Increasing the Cu content to Ti-5Cu raised the UTS to ~1,340 MPa (more than double that of CP-Ti) while maintaining 12% ductility. At Ti-7Cu, the strength further increased to ~1,580 MPa, but the ductility declined to 3%, with specimens fracturing after the yield point. The extracted work-hardening rates (Fig. 1b) reveal that Ti-3Cu exhibited the highest work-hardening capacity, leading to a uniform plastic deformation of ~8%, similar to CP-Ti. In our case, the 8% uniform elongation is higher than most of the conventional alpha-type Ti [23]. In addition, the compressive properties of the as-printed Ti and Ti-Cu alloys were compared, as shown in Fig. S7. The results indicate that the ultimate compressive strength of the as-printed Ti-3Cu alloy is close to 2,000 MPa and increases further with increasing Cu content. This strength is significantly higher than that of Ti-Cu alloys fabricated by conventional casting, forging, and sintering methods [24,25].

We compared the tensile properties, including yield strength (YS), UTS, and tensile ductility (elongation to fracture), from our L-PBF Ti-Cu alloys with other Ti alloys (Fig. 1c and Fig. S8a). These L-PBF Ti-Cu alloys demonstrate a favorable balance of tensile strength and

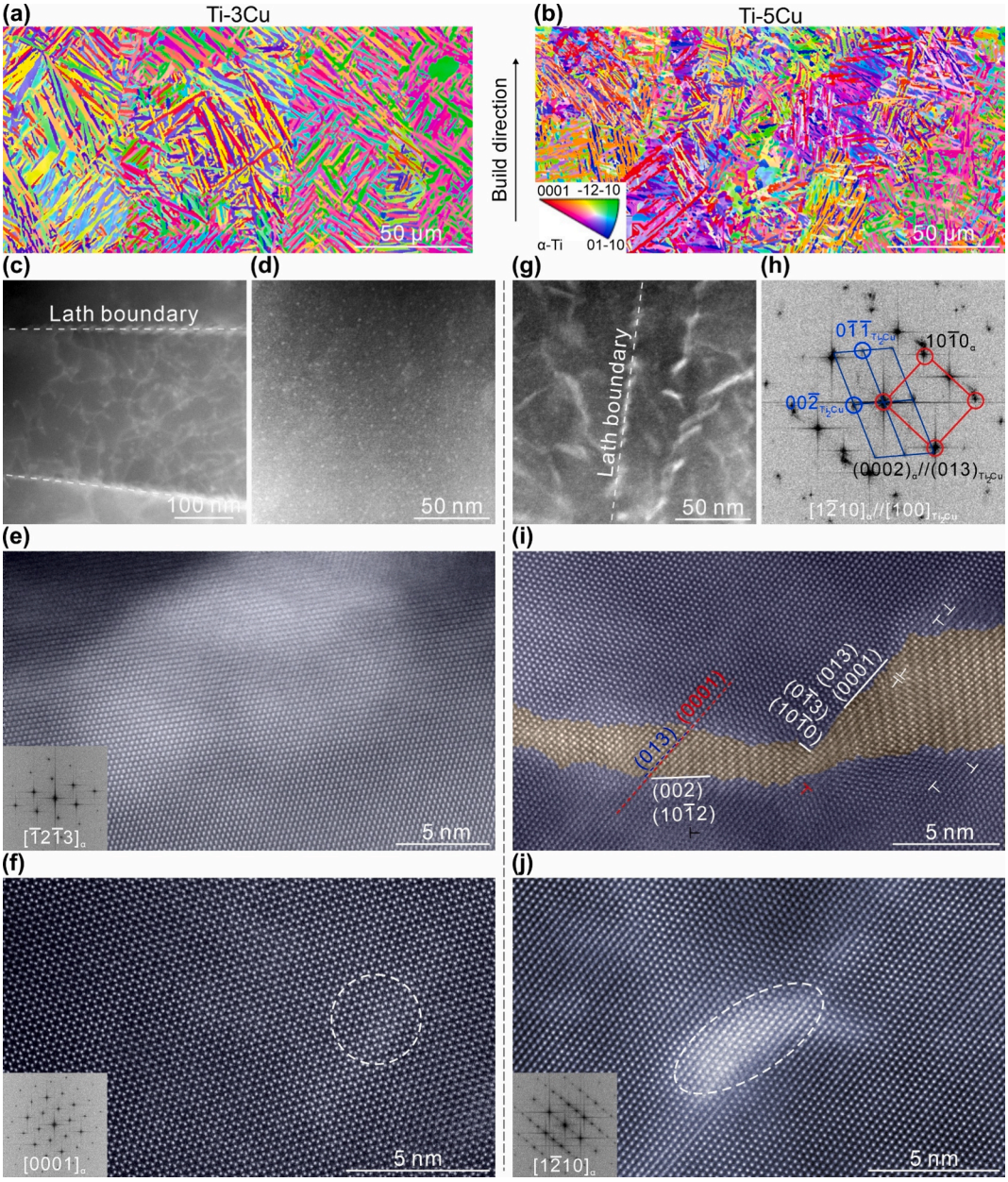

Fig. 2. Microstructures of HSLA Ti fabricated by additive manufacturing. (a and b) EBSD inverse pole figure (IPF) maps showing grain structures of Ti-3Cu (a) and Ti-5Cu (b). (c-f) STEM observations in Ti-3Cu. (c) A LAADF-STEM image showing the Cu-rich nanoprecipitates at lath boundaries. (d) A HAADF-STEM image showing the Cu-rich nanoprecipitates within one lath. (e and f) Atomic resolution HAADF-STEM images taken along a $[\bar{1}\ 2\ \bar{1}\ 3]_{\alpha'}$ zone axis showing coherent HCP Cu-rich nanoprecipitates at lath boundary (e), and a $[0001]_{\alpha'}$ zone axis presenting the coherent HCP Cu-rich nanoprecipitates within the lath (f). (g-j) STEM observations in Ti-5Cu. (g) A HAADF-STEM image presenting bright contrast dotted regions and bright contrast plate-like regions in Ti-5Cu. (h and i) Atomic resolution HAADF-STEM image and the corresponding FFT image presenting the existence of Ti_2Cu nanoprecipitate and the orientation relationship between Ti_2Cu and α-Ti matrix. (j) Atomic resolution HAADF-STEM and the corresponding FFT image presenting the coherent Cu-rich nanoprecipitate within the α lath.

ductility relative to both conventionally manufactured and other AM Ti-Cu alloys [16,26–33]. Furthermore, the tensile properties of our alloys exceed those of benchmark Ti-6Al-4V alloys manufactured by various AM techniques and wrought Ti-6Al-4V alloys [34–38]. We also compared our L-PBF Ti-1.5Cu and Ti-3Cu alloys with other Ti alloys, including α-Ti alloys (Ti-O and Ti-Al) [39,40], β-Ti alloys (Ti-Mo and Ti-Cr) [14,41], and α + β dual-phase Ti alloy (Ti-6Al-4V) [42,43]. The product of strength and ductility of Ti-Cu alloys and Ti64 alloys is compared in Fig. 1d. Ti-3Cu exhibits the highest strength-ductility product among all Ti alloying systems reported to date [16,26–38]. A typical strength-ductility trade-off is observed with increasing solute concentration, following a trend from the lower-right to the upper-left of the strength-ductility map (Fig. 1e and Fig. S8b). Notably, our results show a remarkable increase in strength (from 580 MPa to 940 MPa) without significant loss in ductility, as seen in the transition from CP-Ti to Ti-3Cu. In addition, the strength of our HSLA Ti-Cu outperformed all existing low-alloy Ti and exhibited comparable strength to other high-alloy Ti [12,44–48], as shown in Fig. 1f and Fig. S8c. The material cost of HSLA Ti-Cu alloys in this work was estimated and compared with that of conventional α, near-α, α + β, and β Ti alloys reported in the literature. As shown in Fig. S9, the as-printed Ti-Cu alloys present an outstanding combination of high ultimate tensile strength and relatively low cost compared with most conventional α, near-α, α + β, and β Ti alloys.

Hierarchical microstructure and dual nanoprecipitation

In this work, the O content of the as-fabricated Ti-Cu alloys was measured by a LECO ONH836 Oxygen/Nitrogen/Hydrogen elemental analyzer. The low O content and the similar O levels across all five alloys indicate that the mechanical property differences primarily arise from microstructural variations rather than compositional differences (Table S6). L-PBF Ti-Cu alloys feature a hierarchical microstructure characterized by micron-sized grains containing sub-micron-thick laths and finely dispersed nanoprecipitates. Unlike CP-Ti, which exhibited only irregularly shaped grains (Fig. S10, average grain size ~48 ± 11 μm), all L-PBF Ti-Cu alloys displayed fine basket-weave laths with similar grain morphology (Fig. 2a and b). The average lath thicknesses are approximately 775 ± 54 nm, 475 ± 17 nm, 467 ± 75 nm, and 416 ± 77 nm in Ti-1.5Cu, Ti-3Cu, Ti-5Cu, and Ti-7Cu alloys, respectively (Fig. S11). The reduced lath thickness correlated with increased tensile strength as Cu content increased.

In conventionally processed Ti-Cu alloys, the α phase ($P6_3/mmc$) and intermetallic η phase (Ti_2Cu, I4/mmm) typically form through eutectoid phase transformation. This occurs because Cu's high diffusion rate promotes the eutectoid phase transformation from β to α and η, commonly observed during water quenching and laser directed energy deposition (L-DED) processing [26]. However, X-ray diffraction (XRD) detected only the α′ phase—the same α structure with different Cu content and lattice parameters—in L-PBF Ti-1.5Cu and Ti-3Cu alloys (Figs. S12a-c). This indicates that the neighboring laths in these alloys correspond to different α′ variants. The back-scattered electron (BSE) image of an as-printed Ti-3Cu sample shows α′ laths without bright contrast at their boundaries, indicating no secondary phases are present (Fig. S13).

The martensitic transformation from β to α′ occurs in Ti alloys under rapid cooling. We further confirmed the formation of α′ in L-PBF Ti-1.5Cu and Ti-3Cu alloys through electron backscatter diffraction (EBSD) analysis. The primary misorientation across inter-variant boundaries was dominated by $[\bar{1}0\ 55\ \bar{3}]/63.26°$, which had the highest length fraction among the observed inter-variant boundaries (Fig. S11). Previous studies in Ti alloys [49] indicate that this misorientation is characteristic of diffusionless martensitic transformation, while a dominant 60° inter-variant boundary is typical of diffusive phase transformation from β to α.

For as-printed Ti-3Cu, Fig. 2c-f show its microstructure containing bright-contrast nanoprecipitates. The Cu content in this alloy is 3 wt%, exceeding the solubility limit of Cu in Ti (2.1 wt% in α-Ti at 790 °C) [1], thereby promoting precipitation. Fig. 2c shows a low-angle annular dark-field (LAADF) scanning transmission electron microscopy (STEM) image of laths. Discontinuous, plate-shaped nanoprecipitates are located at the lath boundaries, with an average length of ~16 nm and width of ~5 nm, while the white line segment features inside the laths are primarily dislocations. Fig. 2d shows a high-angle annular dark-field (HAADF)-STEM image taken within a lath, where smaller particle-shaped nanoprecipitates are uniformly dispersed with an average size of ~2 nm. The crystal structures of these two types of nanoprecipitates were analyzed using atomic-resolution HAADF-STEM images. Fig. 2e shows a plate-shaped nanoprecipitate at a lath boundary taken along the $[\bar{1}\ 2\ \bar{1}\ 3]_{\alpha'}$ zone axis. This coherent nanoprecipitate shares the same atomic arrangement as the α′ matrix but appears brighter due to Cu enrichment [50], since Cu has a higher atomic weight than Ti. The inset fast Fourier transform (FFT) pattern reveals a reciprocal space lattice corresponding to an HCP structure. Convergent beam electron diffraction (CBED) further confirms the HCP structure of these nanoprecipitates, as illustrated in Fig. S14. For the particle-shaped nanoprecipitates within the laths, they also exhibit the same atomic arrangement as the α′ matrix, as observed in an HAADF-STEM image along the $[0001]_{\alpha'}$ zone axis (Fig. 2f). The inset FFT pattern and HAADF-STEM images taken along different zone axes (Fig. S15) confirm the HCP structure. These results indicate that both the plate- and particle-shaped Cu-rich nanoprecipitates are coherent with the α′ matrix and henceforth designated as the η′ phase. Moreover, the η′ phase is observed only in samples fabricated using processes with ultrahigh cooling rate, such as L-PBF. Due to the relatively fast diffusion rate of Cu in Ti, the cooling rate achieved during conventional water quenching is not high enough, which promotes the formation of an α + η eutectoid structure, as shown in the BSE images Fig. S16. The bright-contrast laths clearly indicate the presence of the η phase.

In contrast, L-PBF Ti-5Cu and Ti-7Cu primarily comprise α and η phases (Figs. S12d and e), suggesting that higher Cu content promotes diffusive phase transformation. For as-printed Ti-5Cu, Fig. 2g-j show its microstructure containing numerous bright-contrast nanoprecipitates. Discontinuous, plate-shaped nanoprecipitates are present both at the lath boundaries and within the laths, with an average length of ~20 nm and width of ~5 nm. An atomic-resolution HAADF-STEM image taken along the $[1\ \bar{2}1\ 0]_{\alpha}$ zone axis (Fig. 2i) shows an intermetallic η nanoprecipitate (Ti_2Cu, highlighted in orange) at a lath boundary, viewed along the $[100]_{Ti2Cu}$ zone axis. FFT analysis reveals the orientation relationship between the α and η phases as $(0002)_{\alpha}//(0\ 1\ 3)_{Ti2Cu}$ and $<1\ \bar{2}\ 10>_{\alpha}//<100>_{Ti2Cu}$. Additionally, smaller η′ nanoprecipitates within a lath were observed along the $[1\ \bar{2}\ 10]_{\alpha}$ zone axis (Fig. 2j). Compared to the equiaxed particle-shaped η′ nanoprecipitates in Ti-3Cu, those in Ti-5Cu appear more elliptical.

The composition of η′ nanoprecipitates was analyzed using X-ray energy dispersive spectroscopy STEM (XEDS-STEM). Fig. 3a-d show STEM images and corresponding XEDS maps of the η′ nanoprecipitates in L-PBF Ti-3Cu, confirming their Cu-rich nature. Generally, the contrast in STEM-HAADF images is dominated by Z-contrast. Atomic-resolution EDS mapping reveals Cu enrichment while maintaining a coherent crystallographic relationship in the as-printed Ti-3Cu alloy, as shown in Fig. S17. In addition, the EELS-thickness map of the Cu-rich region in the as-printed Ti-3Cu is presented in Fig. S18, confirming the absence of significant local thickness variations. The 3-nm slice (taken through the Cu-rich nanoprecipitate in Fig. 3e) from the atom distribution map of Ti and Cu reveals the η′ nanoprecipitate, as shown by atom probe tomography (APT) in Fig. 3f. The 4.5 at.% Cu iso-concentration surfaces delineate the interface between the matrix and η′ nanoprecipitates. APT analysis indicates that the maximum Cu content in the η′ nanoprecipitates is about 27.5 at.% Cu, and no light elements were detected.

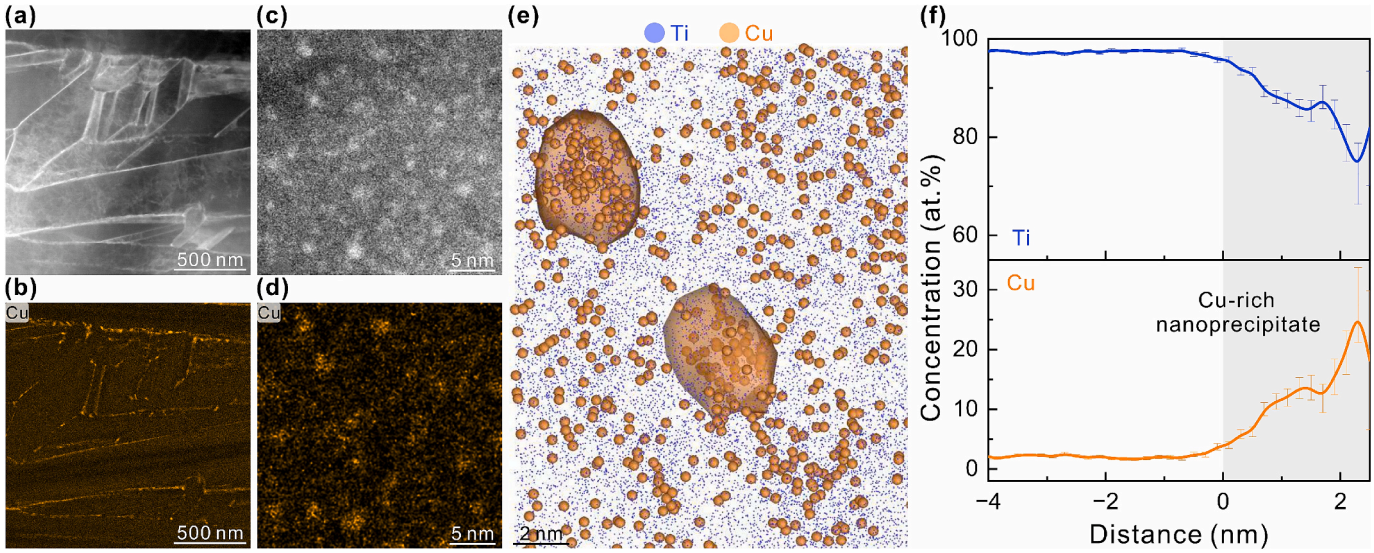

Fig. 3. Nanoprecipitation in Ti-3Cu alloy fabricated by additive manufacturing. (a, b) η′ phases at grain boundaries. (a) LAADF-STEM image and (b) the corresponding XEDS elemental maps of Cu reveal the heterogeneous distribution of Cu in Ti-3Cu alloy. (c, d) η′ phases within the lath. (c) HAADF-STEM image and (d) the corresponding Cu map by STEM-XEDS reveal the Cu distributions within the lath. (e) Three-dimensional reconstructed elemental distributions of Ti and Cu (4.5 at.% iso-concentration) obtained by APT. (f) Linear profiles of Ti and Cu concentrations extracted from the Cu-rich region within the lath (corresponding to the lower Cu-rich nanoprecipitate in (e)).

Moreover, the number density of η′ nanoprecipitates was quantified using large-volume APT data, as shown in Fig. S19. Based on the precipitate number and volume, the number density of η′ nanoprecipitates is estimated to be approximately 2×10^{22} /m^3. These nanoprecipitates transformed into the equilibrium η phase (Ti_2Cu) after heat treatment at 600 °C for 1 h (Fig. S20), indicating that η′ is a precursor to η. APT analysis also confirmed the Cu content of ~30 at.% Cu in the η (Ti_2Cu) phase (Fig. S21). Previous studies reported that coherent nanoprecipitates formed from the decomposition of supersaturated α-Ti solid solution during aging at 400 to 500 °C in Ti-Cu alloys, typically appearing as disk-shaped particles 20 to 40 nm in diameter [51,52]. Here, the η′ nanoprecipitates formed directly through L-PBF rather than aging. The phase transformation pathway from the supersaturated solid solution (S.S.S.S.) of α′ phase in L-PBF Ti-Cu alloys follows

$$\alpha' \text{ (S.S.S.S.)} \rightarrow \eta' \text{ phase} + \alpha'\text{-Ti} \rightarrow \eta' \text{ phase} + \alpha\text{-Ti} + \eta \rightarrow \alpha\text{-Ti} + \eta,$$

with the resulting phase of nanoprecipitates depending on Cu content. At low Cu levels, only η′ nanoprecipitates are present, as observed in Ti-1.5Cu (Fig. S22a) and Ti-3Cu (Figs. 2 and 3). At higher Cu levels (Ti-5Cu), both η′ and η nanoprecipitates are observed (Fig. 2). In Ti-7Cu, η′ nanoprecipitates remain (Fig. S22b), but plate-shaped η nanoprecipitates become dominant (Fig. S23).

It remains unclear whether η′ precipitates can be observed in either conventionally manufactured or additively manufactured Ti-Cu alloys. A previous study indicates that even in a single layer printed L-DED sample, the microstructure of Ti-3Cu and Ti-3.5Cu alloys consists of eutectoid α + η [26,53]. The cooling rate in L-DED is ~10^2-10^4 K/s [54], which is about 100 times lower than that in L-PBF with an ultra-high cooling rate of ~10^5-10^7 K/s [55]. As a result, Ti-Cu fabricated by L-DED is dominated by relatively coarse α lamellae, together with more pronounced Cu-rich intermetallic precipitates (Ti_2Cu) formed under slower solidification conditions and extended thermal exposure. In contrast, the novelty of the present work lies in revealing a hierarchical microstructure consisting of submicron α′/α laths and dual nanoprecipitates, including coherent η′ and incoherent Ti_2Cu nanoprecipitates. In conventional processing, the cooling rate of ~160 °C/s during water quenching is too slow to suppress Cu diffusion in Ti, resulting in the formation of a eutectoid microstructure containing α and η phases [56]. As a result, η′ nanoprecipitates do not form, as confirmed by XRD and HAADF-STEM analyses of arc-melted Ti-Cu specimens (Figs. S12f and S24). Hence, η precipitates dominate in conventional Ti-1.5Cu and Ti-3Cu (Figs. S24a and b), becoming more continuous and coarser with increasing Cu content (Figs. S24c and d). To investigate the formation of η′ nanoprecipitates, we used density functional theory (DFT) calculation to evaluate the relative total energy based on solute–solute separation in a 200-atom Ti supercell. As shown in Fig. S25, Cu-Cu atoms attract each other and prefer a third nearest neighbor (3NN) separation within the Ti matrix, making the formation of the Cu-rich η′ phase energetically favorable.

Discussion

The increased strength and retained ductility in L-PBF Ti-Cu alloys, such as Ti-3Cu and Ti-5Cu, stem from their hierarchical microstructures, which comprise micron-sized grains containing refined α′ or α laths (a few hundred nanometers wide) and finely dispersed nanoprecipitates (as small as ~20 nm for η and ~5 nm for η′ phases). This structural hierarchy effectively impedes dislocation glide and promotes the activation of multiple slip systems, resulting in significant strain hardening that preserves ductility. At the microscale, grain refinement and the dense α′/α lath substructure restrict dislocation mean free paths and promote dislocation accumulation at lath boundaries, providing essential baseline strengthening.

In Ti-3Cu, which primarily contains η′ nanoprecipitates, was examined first. The bright-field and dark-field STEM images at 12% strain (Fig. 4a and Figs. S26a-c) revealed plenty of curved <a> dislocations within the α′ laths, indicative of their low activation shear stress. In addition, a number of straight, parallel <c+a> dislocations were observed, accommodating local deformation mismatches near lath boundaries and nanoprecipitates (as indicated by the white arrows), despite their high activation shear stress. At an applied strain of 22%, <c+a> dislocations became more prominent and entangled near the fracture surface (Fig. 4b and Figs. S26d-f). This suggests that η′ nanoprecipitates temporarily hindered but did not completely block dislocation motion. Atomistic simulations, discussed later, indicate that increased shear stress enables dislocations to cut through η′ nanoprecipitates. Repeated dislocation cutting on the same slip plane weakens local bonding [57], promoting planar slip [58], as evidenced by

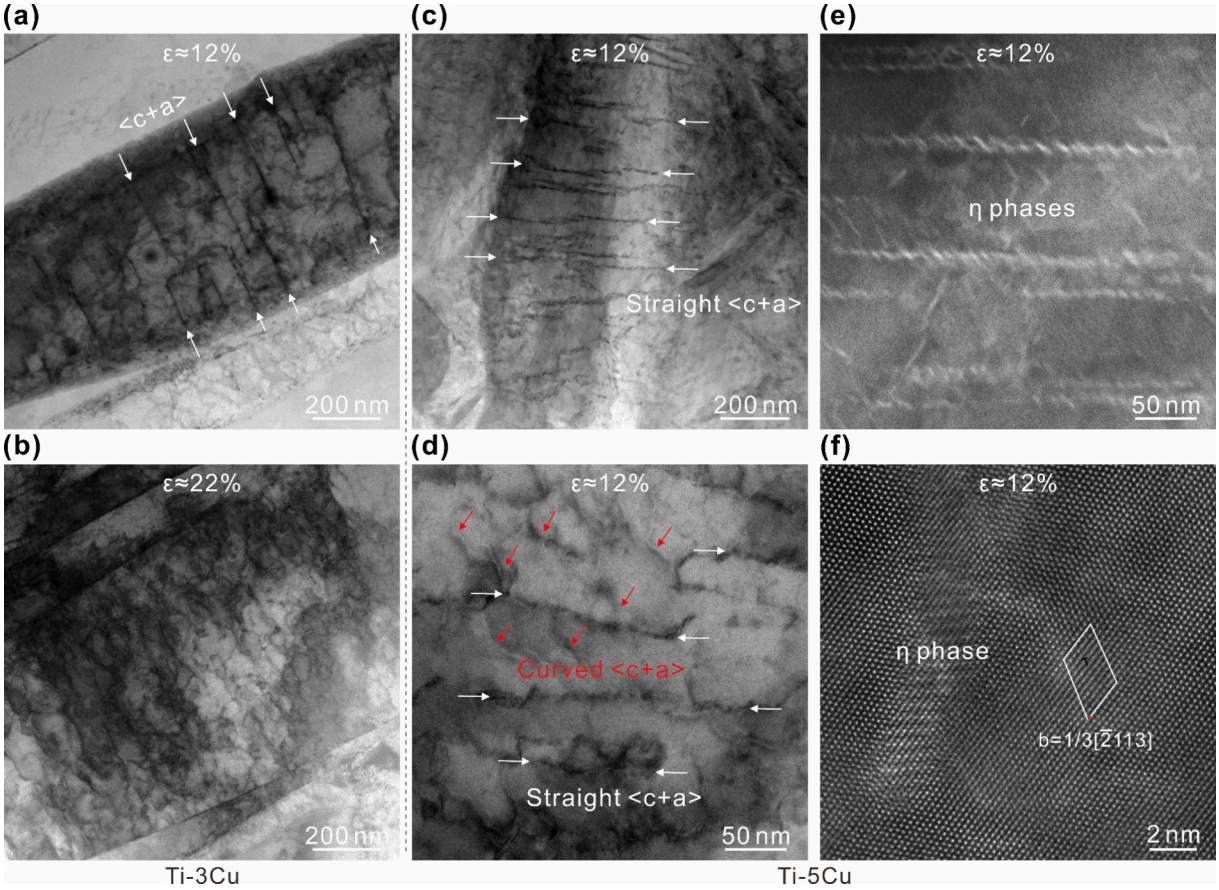

Fig. 4. Deformation mechanisms of HSLA Ti. (a and b) STEM observations of dislocations during plastic deformation of Ti-3Cu containing the η′ phase. (a) A bright-field STEM image showing dislocations in the deformed sample (~12% strain). (b) A bright-field STEM image showing dislocations in the fractured sample (~22% strain). The observed regions are near the tensile fracture surface. (c-f) TEM observations of fractured Ti-5Cu samples (~12% strain) containing the η′ and Ti_2Cu η nanoprecipitates. (c) A bright-field TEM image showing dislocations pinned by Ti_2Cu nanoprecipitates within an α lath. (d) A bright-field STEM image showing dislocations between Ti_2Cu arrays. (e) A HAADF-STEM image showing straight Ti_2Cu nanoprecipitates arrays. (f) Atomic resolution HAADF-STEM image along [1 $\bar{2}$1 0] zone axis showing the dislocation types.

the parallel dislocation pattern in Fig. 4a. With increasing strain, planar-slip dislocations appear curved, indicative of enhanced cross-slip and multi-slip, which enhance strain hardening and contribute to the retained ductility in L-PBF Ti-3Cu.

In Ti-5Cu, containing both η and η' nanoprecipitates, dislocation behavior differed from that in Ti-3Cu. At 12% strain near the fracture surface (Fig. 4c), straight, parallel <c+a> dislocations were observed, as indicated by the white arrows. However, detailed examination (Fig. 4d and Figs. S27a and b) revealed a mixture of dislocation morphologies, including straight <c+a> and curved <c+a> dislocations, marked by white and red arrows, respectively. In regions containing η nanoprecipitates, these nanoprecipitates aligned in rows, as shown in the HAADF-STEM image in Fig. 4e. These nanoprecipitates strongly impeded <c+a> dislocation motion, effectively pining them, as shown in Fig. 4d. However, in regions between these blocked <c+a> dislocations that were free of η nanoprecipitates, the curved <c+a> dislocations were activated and dominated. The atomic-resolution STEM-HAADF image in Fig. 4f identified dislocations with Burgers vectors of 1/3[$\bar{2}$ 113]. These findings indicate that when η nanoprecipitates block partial <c+a> dislocations, additional <c+a> dislocations are activated to glide in η-free regions. Compared to the shearable η' nanoprecipitates in Ti-3Cu, the aligned, hard-to-shear η nanoprecipitates in Ti-5Cu strongly inhibit <c+a> dislocation motion, resulting in an ultra-strong alloy with a ~35% increase in yield strength relative to Ti-3Cu. Meanwhile, the finely dispersed η' nanoprecipitates, present at a high number density in Ti-5Cu, contribute to strengthening while maintaining ductility up to 12%, sufficient for many practical applications.

Specifically, MD simulations were conducted to further investigate the strengthening effect of η′ nanoprecipitates in Ti-Cu alloys (Fig. 5 and Fig. S28). As shown in Fig. 5a, an edge <a> dislocation is impeded by a periodic array of spherical η′ nanoprecipitates with a spacing of 20 nm and a diameter of 4 nm, based on the APT results in Fig. 3e and Fig. S19. The MD stress–strain curves in Fig. 5b show that a high critical shear stress (~570 MPa) is needed for the dislocation to break away this array, compared to ~390 MPa in CP-Ti, demonstrating the strong pinning effect of η′ nanoprecipitates. The influence of nanoprecipitate spacing on strengthening was also evaluated. Fig. 5 c and Fig. S29 reveal that decreasing the spacing (S) increases the shear resistance. Classical strengthening theory [59], which considers non-shearable pinning particles, approximates the strengthening effect as $\tau_c = \tau_c^0 + 2T\cos\phi_c/bS$, where τ_c is the shear resistance with the nanoprecipitate spacing S, τ_c^0 is the shear resistance in CP-Ti, T is the line tension, $\phi_c = \pi/6$ is the critical angle at which dislocation breakaway occurs, and b is the Burgers vector length, respectively. The fit in Fig. 5c yields $T = \alpha Gb^2$, with $\alpha = 0.3$, leading to an estimated shear resistance increase $\Delta\tau_c$ of ~180 MPa for $S = 20$ nm. For polycrystalline Ti-Cu, this translates to a yield stress increase $\Delta\sigma_y \approx 3\Delta\tau_c = 540$ MPa [60], with a Taylor factor of 3. Given that this value is obtained at a high strain rate of $10^8\ s^{-1}$ through MD simulations, the yield stress increases at the conventional experimental strain rate $10^{-3}\ s^{-1}$ can be estimated as $\Delta\sigma =$

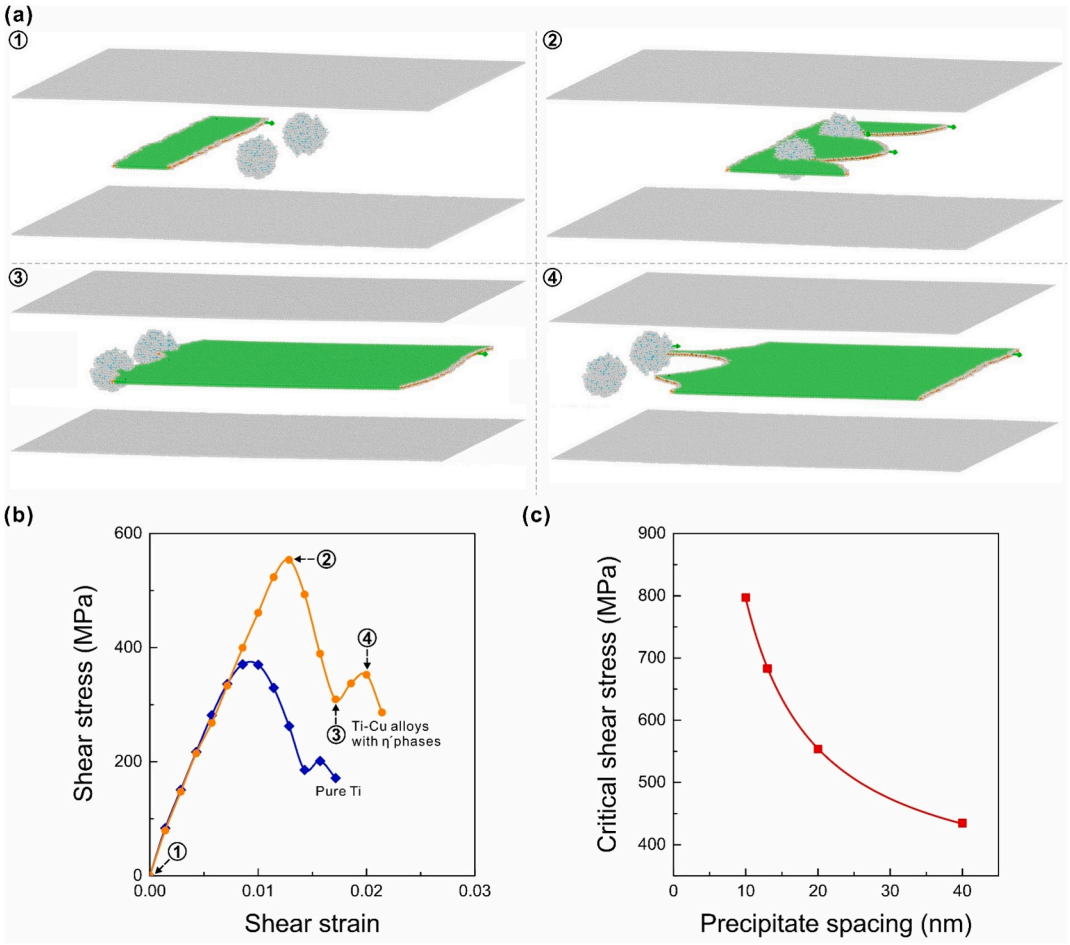

Fig. 5. MD simulation of the pinning effect of η′ phases on dislocation motion in Ti-Cu alloys. (a) Atomistic configurations along the stress–strain curve of dislocation cutting through an array of η′ phases with spacing $S = 20$ nm and diameter $D = 4$ nm, and their corresponding stress/strain values are plotted as black circles of the orange curve in (b). (b) Stress–strain curves of edge dislocation cutting through an array of η′ phases with spacing $S = 20$ nm and diameter $D = 4$ nm. (c) Variations of critical shear stress with different η′ phases spacing for the fixed diameter $D = 4$ nm.

$\left(10^{-3}/10^{8}\right)^{m}\Delta\sigma_y = 325$ MPa, where the strain rate sensitivity is chosen as 0.02 for α-titanium alloys [61]. Additionally, Fig. S29 shows η′ nanoprecipitates are shearable, allowing plastic strain accommodation through dislocation pinning and cutting, which enhances both strength and ductility. Hence, the above estimate of $\Delta\sigma_y$ represents an upper limit, as it does not account for the effects of shearable nanoprecipitates and high loading rates in MD. Fig. S30 and Fig. S31 further illustrate the effect of η′ nanoprecipitates on <c+a> dislocation motion. Although some debris is left after a <c+a> dislocation cuts through η′ nanoprecipitates, these finely dispersed obstacles significantly hinder dislocation motion, contributing to strengthening.

In addition, Ti-5Cu exhibits a higher work-hardening rate than Ti-3Cu at true strains below ~0.035, which can be attributed to the strong dislocation-pinning effect of η nanoprecipitates. Beyond this strain, the work-hardening rate of Ti-3Cu surpasses that of Ti-5Cu, likely due to enhanced cross-slip and the activation of multiple slip systems, which promote more homogeneous plastic deformation. In contrast, the work-hardening rate of Ti-5Cu decreases rapidly beyond this point and drops sharply prior to necking, whereas Ti-3Cu shows a more gradual and continuous decline. In the early deformation stage, plastic strain is primarily accommodated by easy <a> dislocation glide within soft channels between η arrays or in regions containing shearable η′ precipitates. With increasing strain, dislocation pile-up at the hard η arrays generates local stress concentrations sufficient to activate <c+a> slip systems, enabling coordinated c-axis deformation and preventing premature brittle fracture. Consequently, the hierarchical arrangement of hard η arrays and soft η′-containing channels produces a composite-like deformation behavior, where the η arrays provide high strength and the soft channels sustain plastic flow to preserve ductility.

Moreover, the fractured surface morphologies of L-PBF Ti-Cu alloys were examined by scanning electron microscopy (SEM). Ti-1.5Cu and Ti-3Cu alloys predominantly exhibited dimpled surfaces, characteristic of ductile fracture (Fig. S32a and b). In contrast, Ti-5Cu and Ti-7Cu alloys displayed a mix of dimples and cleavage features, reflecting a combination of high strength and ductility. Notably, the fracture surfaces of Ti-7Cu were largely dominated by quasi-cleavage features (Fig. S32c and d), correlating with its markedly reduced ductility.

Conclusions

Leveraging the effects of cooling and diffusion rates on phase transformation and solute composition, additive manufacturing [62] enables the creation of hierarchical microstructures in low-alloy Ti systems. These microstructures feature micron-sized grains containing refined α′ or α laths (a few hundred nanometers wide) and finely dispersed nanoprecipitates (as small as ~20 nm for η and ~5 nm for η′ phases), with the alloy composition dictating the specific phases formed. This structural hierarchy effectively impedes dislocation glide and activates multiple slip systems, leading to significant strengthening and hardening while preserving ductility. Notably, the extreme processing conditions of L-PBF, including steep temperature gradients and rapid cooling rates, largely suppress diffusive phase transformations, resulting

in sub-micron-thick basket-weave α′ laths with finely dispersed coherent η′ nanoprecipitates at lath boundaries and within laths. This microstructure in Ti-3Cu yields a UTS of ~940 MPa and an elongation to failure of ~22%. Increasing Cu content allows for further tuning hierarchical microstructures and mechanical properties. For example, enhanced Cu diffusion in Ti-5Cu promotes diffusive phase transformation during L-PBF cooling, producing sub-micron-thick basket-weave α laths with dual nanoprecipitation: a mixture of incoherent η nanoprecipitates along with coherent η′ nanoprecipitates. This microstructure raises the UTS to ~1,340 MPa while maintaining 12% ductility. These unique microstructures and exceptional strength-ductility combinations are rarely attainable in HSLA Ti through conventional processing. We anticipate that additive manufacturing holds transformative potential for developing a wide range of high-performance, sustainable low-alloy Ti systems. Furthermore, the incorporation of Cu serves to impart antibacterial properties, which mitigate bacterial adhesion, and biofilm formation. This renders Ti-Cu alloys particularly suitable for antimicrobial implantable devices, where both mechanical strength and bacterial resistance are of critical importance.

Methods

Materials for the preparation of Ti and Ti-Cu alloys. The additive manufacturing process utilized two variants of high-purity argon-gas-atomized powders, comprising pure titanium and pure copper, characterized by particle sizes ranging from 15 to 53 μm. These powders were procured from Avimetal Additive Manufacturing Co., Ltd. The Ti-Cu alloys were intentionally composed of different ratios, namely Ti-1.5 wt% Cu, Ti-3 wt% Cu, Ti-5 wt% Cu, and Ti-7 wt% Cu, which are hereafter denoted as Ti-1.5Cu, Ti-3Cu, Ti-5Cu, and Ti-7Cu, respectively. As a point of reference for comparative purposes, pure titanium was also integrated into the study. Each set of powders designated for a specific Ti-Cu alloy composition underwent a meticulous weighing process and was subsequently stored within sealed plastic containers. To ensure uniformity in composition, these powders were subjected to mechanical blending using a 3D-shaker (Turbula® T2F, WAB Group) operating at 150 rpm for a duration of 2 h, all conducted at ambient temperature.

For the traditional vacuum-arc melting process, high-purity nuggets of titanium and copper were sourced from Beijing Ryubon New Materials Technology, Ltd. This process was repeated for the same compositions, encompassing pure titanium and Ti-1.5Cu, Ti-3Cu, Ti-5Cu, and Ti-7Cu alloys. Each alloy composition was subjected to meticulous weighing and underwent mechanical blending as part of the preparatory steps for the subsequent vacuum-arc melting procedure.

Preparation of Ti and Ti-Cu alloys by additive manufacturing. Additive manufacturing of Ti-Cu alloys was performed using laser powder bed fusion (L-PBF) on an SLM 125HL machine equipped with a single laser (SLM Solutions Group). To maintain a controlled environment, the entire fabrication process was executed within a protective argon atmosphere. The fabrication of Ti-Cu alloys was divided into two stages: an initial exploration of formability and a final parameter optimization for sample preparation. A laser spot diameter of 80 μm, layer thickness of 30 μm, hatch spacing of 105 μm, and a layer rotation angle of 90° were used in this work. During the stage of formability exploration, the laser power was varied from 150 to 350 W with a step size of 50 W, while the scanning speed was adjusted from 500 to 1400 mm/s with a step size of 300 mm/s. Based on systematic evaluation of formability and tensile properties (Figs. S1-5), an optimal processing condition with a laser power of 350 W and a scanning speed of 800 mm/s was determined for final sample fabrication.

Preparation of Ti and Ti-Cu alloys by arc melting. Pure Ti and Ti-Cu alloy ingots were produced through arc-melting within a vacuum environment, employing a vacuum arc melter (WK-II) provided by Physcience Opto-electronics Co., Ltd. in Beijing, China. Throughout the arc melting process, the furnace was maintained under conditions of low oxygen concentration, achieved by evacuating the chamber to a pressure of 5×10^{-3} Pa and subsequently purging it with argon to reach a pressure of 0.5 Pa. Furthermore, all ingots underwent a meticulous re-melting process, repeated five times, thereby guaranteeing the homogeneity of element distribution across the material.

Heat treatments of Ti-Cu alloys. The as-printed Ti-3Cu alloy was heat treatment at 600 °C for 1 h and then furnace cooling to study the thermal stability of the η′ phase. All samples were inside a vacuum-sealed tube and then conducted with a tube furnace. In addition, a beta solution treatment was performed on the Ti-3Cu alloys. The as-printed and as-cast Ti-3Cu alloys were first sealed in a quartz tube filled with Ar gas to avoid oxidation. A beta-treatment was conducted at 1000 °C for 2 h. After that, the tube was quenched in cold water at room temperature.

XRD measurements. The phase compositions of both Ti and Ti-Cu alloys, obtained via both additive manufacturing and arc melting processes, were analyzed using X-ray diffraction (XRD). XRD samples were initially prepared by cutting foils from the as-printed parts using wire-cut electrical discharge machining. These foils were subsequently subjected to mechanical polishing to achieve the desired surface quality. XRD measurements were performed utilizing a Rigaku SmartLab diffractometer equipped with a copper target. The measurements were conducted at an operating power of 9 kW (45 kV, 200 mA) within a scanning range spanning from 20° to 100°, with a step size of 0.02°.

EBSD and BSE observations. The microstructures of Ti-Cu alloys, fabricated using additive manufacturing, were characterized through EBSD and BSE. The EBSD and BSE experiments were conducted using a ThermoFisher Verios 5UC field-emission scanning electron microscope (SEM) equipped with an Oxford EBSD system and BSE detector. To prepare the EBSD and BSE samples, foils were initially cut along the building direction from the as-printed parts using WEDM. Subsequently, mechanical polishing was employed to refine the sample surfaces, followed by polishing using an argon ion polishing system (Gatan PECS II 685). During the EBSD and BSE observations, the microscope operated at a voltage of 20 kV, and the EBSD measurements were taken at a step size of 40 nm.

TEM and STEM experiments. TEM experiments were conducted using a JEOL JEM-2200FS microscope operated at 200 kV. STEM characterization was performed using Titan Themis-Z and Thermo Fisher Spectra 300 double-corrected microscope equipped with Chem-iSTEM (Super-X) EDS detectors and a Gatan Quantum ER/965 GIF dual EELS system working at 300 kV. All compositional mappings were conducted under a beam current of 200 pA and sufficiently long data collection times to ensure > 100,000 counts to minimise statistical errors. A semi-convergence angle of 25.1 mrad was used to acquire atomic resolution images. Bright-field (BF) STEM images were collected in the (semi-) angle range of 0–10 mrad. The STEM high-angle annual dark-field (HAADF) images were obtained with a collection angle of 76–200 mrad. A beam current of 50 pA, a dwell time of 10 μs per pixel, and an image size of 1024 × 1024 pixel were utilized. Moreover, the CBED observations were conducted by a 200 kV Talos F200X TEM. In addition, electron energy-loss spectroscopy (EELS) was performed. A high-energy electron beam was transmitted through an electron-transparent specimen, and the energy losses of inelastically scattered electrons were analyzed using a post-column EELS spectrometer.

APT analysis. Needle-shaped specimens from the as-printed Ti-3/5Cu alloys for APT were prepared using the lift-out method and were subsequently annular-milled in a Thermofisher G4 Hydra Plasma FIB-SEM. APT experiments were carried out on a CAMECA Local Electrode Atom Probe 4000X Si microscope, which features a picosecond-pulse ultraviolet laser at a wavelength of 355 nm. The experiment conditions were set as follows: a base temperature of 50 K, a laser frequency of 200 kHz, and a laser energy of 40 pJ. Data was reconstructed using the AP suite 6.1.0, with default parameters for detector efficiency (0.57), ICF (1.65), and k_f (3.30). The error bars (σ_i) shown in the 1D concentration profiles were calculated as: $\sigma_i = C_i(1 - C_i)N$, where $C_i = N_i/N$, N_i represents the number of i solute ions/atoms, and N represents the total

number of all ions/atoms with the given bin [63,64]. The bin width was defined as 0.2 nm.

Uniaxial tensile and compressive tests. The tensile properties of Ti and Ti-Cu alloys, manufactured through both additive manufacturing, were assessed using a ZwickRoell Z020 TEW universal testing machine, equipped with a laser extensometer. Tensile samples were prepared by cutting dog-bone-shaped specimens from the as-printed parts using WEDM. Subsequently, these specimens underwent mechanical polishing to ensure suitable surface quality. The gauge section of these specimens had standardized dimensions of 10 mm in length, 2 mm in width, and 2 mm in thickness, following the ASTM guidelines. Tensile tests were conducted at a strain rate of 10^{-3} s^{-1}, with strain measurements recorded using a noncontact laser extensometer. To ensure the reproducibility of the experimental results, each group of Ti and Ti-Cu alloys underwent three repetitions of tensile testing. Following the tensile tests, the fracture morphologies were examined using a Tescan Mira high-resolution analytical SEM. This SEM was equipped with a high brightness field emission electron source and operated at a voltage of 20 kV to capture detailed images of the fracture surfaces. Moreover, compression tests were conducted using an Instron 68TM-50 testing machine at room temperature with a strain rate of 10^{-3} s^{-1}. For the as-printed Ti and Ti-Cu alloys, the compression direction was aligned perpendicular to the build direction. Cylindrical compression specimens with dimensions of Ø2 mm × 3 mm were prepared and polished using successive grades of SiC paper to remove surface defects before testing.

DFT calculations. Density functional theory (DFT) calculations were performed using the generalized gradient approximation [65] and the projector augmented-wave method, as implemented in the VASP code [66]. A cutoff energy for plane-wave basis sets of 500 eV was applied. The Monkhorst-Pack k-points were meshed by 2 × 2 × 2 for the 200-atom (5a × 5a × 4c) α-Ti supercell. Atomic relaxation was allowed until the forces converged to less than 0.01 eV $Å^{-1}$.

MD simulations. Fig. S28 presents the simulation setup for ⟨0001⟩ {11$\bar{2}$0} edge dislocation motion in the basal plane. The simulation cell has dimensions of 43 nm × 40 nm × 14 nm and contains a total of ~1,430,000 atoms. Periodic boundary condition is applied along the Y-[$\bar{1}$100] dislocation line and dislocation motion direction (X-[11$\bar{2}$0]). Z-[0001] is traction-free. Two 1.5-nm-thick layers are fixed at the top and bottom surfaces in the Z-[0001] direction. Shear load is applied by imposing a displacement-controlled boundary condition on the top and bottom slabs to maintain a constant shear strain rate of 2×10^8 s^{-1}. The simulations are performed using LAMMPS at room temperature (i.e., 300 K) [67]. The modified embedded atom method (MEAM) potential of the Ti-Cu system is employed [68]. A spherical with a diameter of 6 nm is selected at a certain distance from the edge dislocation to introduce 10% Cu, and the interval between each precipitate is 20 nm. The system is held at a temperature of 300 K in the canonical ensemble (NVT). The visualization tool OVITO is used to perform common neighbor analysis and dislocation analysis to clearly show the edge dislocation [69].

Fig. S30 presents another atomistic configuration of the MD simulation cell containing a <c+a> left-hand screw dislocation. The simulation cell, with dimensions of 45.5 nm × 21.9 nm × 6.1 nm, comprises approximately 348,000 atoms. Periodic boundary conditions are applied along the Z-[1$\bar{2}$13] dislocation line, while the X-[10$\bar{1}$0] and Y-axis are maintained traction-free. Additionally, two 1.5-nm-thick layers are fixed at the top and bottom surfaces along the Y direction. A shear load is applied to maintain the constant shear strain rate of 2.3×10^8 s^{-1}, consistent with the aforementioned configuration. A series of spheres with a diameter of 3 nm and spacing of 3 nm are selected at a certain distance from the screw dislocation to introduce 20% Cu. All the other simulation parameters and method remained identical to those described for Fig. S28.

Author contributions.

Z.C. and S.R. conceptualised and supervised the project. C.R. printed samples and performed the mechanical experiments and essential characterization. H.W. performed HAADF-STEM experiments. T.Z., D. C., and J.G., performed MD simulations. X.C. performed DFT calculations. H.C. performed APT experiments. Z.S., H.S., and Y.R. assisted in electron microscopy experiments. C.R., H.W., H.L., C.W., C.F.C., K.C., and X.L. analyzed the data and discussed the results. All authors reviewed and contributed to the final manuscript.

All data needed to evaluate the conclusions in the paper are present in the paper and/or the Supplementary Information. Additional data related to this paper may be requested from the authors.

CRediT authorship contribution statement

Chuanxi Ren: Writing – original draft, Methodology, Investigation, Data curation. **Hao Wang:** Writing – original draft, Investigation, Data curation. **Xiangyuan Cui:** Methodology, Investigation. **Jinjin Guo:** Formal analysis, Data curation. **Hansheng Chen:** Methodology, Investigation, Data curation. **Zizheng Song:** Methodology, Investigation. **Hengchao Shi:** Investigation, Data curation. **Yating Ran:** Methodology, Investigation, Data curation. **Chunjin Wang:** Methodology, Investigation. **Chi Fai Cheung:** Supervision, Resources, Investigation. **Hongwei Liu:** Methodology, Investigation. **Kang Cheung Chan:** Resources, Methodology, Investigation. **Xiaozhou Liao:** Supervision, Methodology, Conceptualization. **Ting Zhu:** Writing – review & editing, Resources, Conceptualization. **Dengke Chen:** Writing – original draft, Resources, Methodology, Conceptualization. **Simon P. Ringer:** Resources, Investigation, Conceptualization. **Zibin Chen:** Writing – review & editing, Resources, Investigation, Data curation, Conceptualization.

Declaration of competing interest

The authors declare that they have no known competing financial interests or personal relationships that could have appeared to influence the work reported in this paper.

Acknowledgements

We thank Tab Cheng for sample preparation, Ruien Hu, Qi Liu, Xingdong Dan, Shengxi Jin, Yixuan Sun, and Bo-Rung Chen (a visiting student in Professor Ringer's group) for experimental support. We acknowledge the University Research Facility in 3D Printing (U3DP) at the Hong Kong Polytechnic University, the Sydney Microscopy & Microanalysis at the University of Sydney, which is a node of Microscopy Australia, Sydney Informatics Hub (the University of Sydney) and the National Computational Infrastructure (NCI) for the facilities and technical assistance. Both Microscopy Australia and the NCI are supported by the Australian Government's National Collaborative Research Infrastructure Scheme. Z.C and C.R acknowledge the funding support from Shenzhen Municipal Science and Technology Innovation Commission (Project code: SGDX20230821092100002), PolyU Research and Innovation Office (Project code: ZZXN, CDPD, CD9E, and CDLQ), the Postdoc Matching Fund Scheme of The Hong Kong Polytechnic University (PolyU) (Project code: W23A and W31P), the PolyU-SCUT Joint Research Centre for Advanced and Green Composite Materials, and the funding support for the State Key Laboratories in Hong Kong from the Innovation and Technology Commission of the Government of the Hong Kong Special Administrative Region, China. D.C acknowledges the support from the National Natural Science Foundation of China (No. 12272224), and the Natural Science Foundation of Shanghai (No. 22ZR1428500). H. C acknowledges the AXA Post-Doctoral Fellowship funded by AXA Foundation for Human Progress. S. R acknowledges funding support from the Australian Research Council (DP200100940).

Appendix A. Supplementary material

Supplementary data to this article can be found online.

Appendix B. Supplementary data

Supplementary data to this article can be found online at https://doi.org/10.1016/j.mattod.2026.103329.

Data availability

Data will be made available on request.

References

[1] M.R. Akbarpour, et al., Prog. Mater Sci. 127 (2022) 100933.
[2] M. Rashid, Science 208 (1980) 862–869.
[3] J. Yao, et al., Addit. Manuf. 94 (2024) 104496.
[4] S. Ahangarani, et al., Appl. Surf. Sci. 254 (2007) 1427–1435.
[5] L. Simoni, et al., Int. J. Hydrogen Energy 46 (2021) 25738–25751.
[6] C. Leyens, Peters M., Titanium and Titanium alloys: Fundamentals and Applications, Wiley-VCH Verlag, 2003.
[7] T. Song, et al., Nature 618 (2023) 63–68.
[8] X. Wu, et al., Proc. Natl. Acad. Sci. U. S. A. 112 (2015) 14501–14505.
[9] C. Zhang, et al., Nat. Commun. 14 (2023) 1397.
[10] P. Kumar, et al., Acta Mater. 154 (2018) 246–260.
[11] R.R. Boyer, Mater. Sci. Eng. A 213 (1996) 103–114.
[12] I. Polmear, et al., Light Alloys: Metallurgy of the Light Metals, Butterworth-Heinemann, 2017.
[13] J. Niu, et al., Mater. Sci. Eng. C 122 (2021) 111917.
[14] M. Hattori, et al., Dent. Mater. J. 29 (2010) 570–574.
[15] M. Takahashi, et al., Dent. Mater. J. 21 (2002) 270–280.
[16] A.O.F. Hayama, et al., Mater. Des. 55 (2014) 1006–1013.
[17] T. Hong, et al., Phys. Rev. B 41 (1990) 12462–12467.
[18] H. Donthula, et al., Acta Mater. 168 (2019) 63–75.
[19] X. Zhao, et al., Acta Biomater. 8 (2012) 2392–2400.
[20] Z. Wang, et al., Sci. Adv. 6 (2020) eaba9543.
[21] H. Wang, et al., Mater. Today 61 (2022) 11–21.
[22] N. Ren, et al., Nat. Commun. 14 (2023) 7990.
[23] Y. Yang, et al., Nat. Commun. 16 (2025) 10833.
[24] E. Zhang, et al., Mater. Sci. Eng. C 69 (2016) 1210–1221.
[25] E. Zhang, et al., Mater. Sci. Eng. C 69 (2016) 760–768.
[26] D. Zhang, et al., Nature 576 (2019) 91–95.
[27] Q. Wang, et al., J. Alloys Compd. 885 (2021) 161032.
[28] Y. Ren, et al., Mater Charact 192 (2022) 112217.
[29] H. Liu, et al., J. Mater. Sci. Technol. 132 (2023) 100–109.
[30] M. Bao, et al., Bioact. Mater. 3 (2018) 28–38.
[31] S.A. Mantri, et al., Addit. Manuf. 32 (2020) 101067.
[32] Y. Alshammari, et al., J. Mech. Behav. Biomed. Mater. 95 (2019) 232–239.
[33] M. Kikuchi, et al., Dent. Mater. 19 (2003) 174–181.
[34] C. Qiu, et al., Mater. Sci. Eng. A 578 (2013) 230–239.
[35] H.D. Nguyen, et al., J. Mater. Res. Technol. 18 (2022) 4641–4661.
[36] N. Hrabe, Quinn T, Mater. Sci. Eng. A 573 (2013) 271–277.
[37] B.E. Carroll, et al., Acta Mater. 87 (2015) 309–320.
[38] T. Vilaro, et al., Metall. Mater. Trans. A 42 (2011) 3190–3199.
[39] Y. Chong, et al., Sci. Adv. 6 (2020) eabc4060.
[40] S.S. Youssef, et al., Mater. Sci. Eng. A 819 (2021) 141513.
[41] J.W. Lu, et al., Mater Charact 84 (2013) 105–111.
[42] K.M. Li, et al., Mater. Des. 215 (2022) 110491.
[43] W.F. Ho, J. Alloys Compd. 464 (2008) 580–583.
[44] Y. Zhu, et al., Nat. Mater. 21 (2022) 1258–1262.
[45] R. Duan, et al., Addit. Manuf. 37 (2021).
[46] A. Zafari, et al., J. Mater. Sci. Technol. 105 (2022) 131–141.
[47] C.L. Li, et al., J. Alloys Compd. 550 (2013) 23–30.
[48] O.M. Ivasishin, et al., J. Alloys Compd. 457 (2008) 296–309.
[49] H. Beladi, et al., Acta Mater. 80 (2014) 478–489.
[50] C. Kübel, et al., Microsc. Microanal. 11 (2005) 378–400.
[51] J. Williams, et al., Metall. Trans. 2 (1971) 1139–1148.
[52] M. Mitsuhara, et al., Metall. Mater. Trans. A 47 (2016) 1544–1553.
[53] K. Sun, et al., J. Alloys Compd. 1013 (2025) 178580.
[54] S.J. Wolff, et al., Acta Mater. 132 (2017) 106–117.
[55] T. DebRoy, et al., Nat. Mater. 18 (2019) 1026–1032.
[56] S.A. Souza, et al., Mater. Sci. Eng. C 29 (2009) 1023–1028.
[57] D. Lunt, et al., Acta Mater. 129 (2017) 72–82.
[58] Q.J. Li, et al., Nat. Commun. 10 (2019) 3563.
[59] A. Argon, Strengthening Mechanisms in Crystal Plasticity, Oxford University Press, New York, 2007.
[60] T. Zhu, Li J, Prog. Mater Sci. 55 (2010) 710–757.
[61] W.F. Hosford, Mechanical Behavior of Materials, Cambridge University Press, New York, 2005.
[62] D. Herzog, et al., Acta Mater. 117 (2016) 371–392.
[63] S. Wallis, J. Quant. Linguist. 20 (2013) 178–208.
[64] D.J. Larson, et al., Local Electrode Atom Probe Tomography: a User's Guide, Springer, New York, 2013.
[65] J.P. Perdew, et al., Phys. Rev. Lett. 77 (1996) 3865–3868.
[66] G. Kresse, Joubert D, Phys. Rev. B 59 (1999) 1758–1775.
[67] S. Plimpton, J. Comput. Phys. 117 (1995) 1–19.
[68] A.S.M. Miraz, et al., Mater. Des. 196 (2020) 109123.
[69] A. Stukowski, Model. Simul. Mater. Sci. Eng. 18 (2009) 015012.